
Article:
Han, Yaofei, Wu, Xuanqin, He, Guofeng et al. (2 more authors) (2020) Nonlinear magnetic field vector control with time-varying parameters for high-power electrically excited synchronous motor. IEEE Transactions on Power Electronics. pp. 11053-11063. ISSN: 0885-8993

https://doi.org/10.1109/TPEL.2020.2977390

This article has been accepted for publication in a future issue of this journal, but has not been fully edited. Content may change prior to final publication. Citation information: DOI 10.1109/TPEL.2020.2977390, IEEE Transactions on Power Electronics

Nonlinear Magnetic Field Vector Control With Dynamic-variant Parameters for High-power Electrically Excited Synchronous Motor

Yaofei Han, *Member, IEEE*, Xuanqin Wu, Guofeng He, *Member, IEEE*, Yihua Hu, *Senior Member, IEEE*, and Kai Ni, *Member, IEEE*

Abstract: **Identifying the air-gap flux is a prerequisite for realizing the decoupling control between air-gap flux and torque in an electrically excited synchronous motor (EESM) vector control system. For the nonlinear problem of EESM, the frequency response function method is introduced to analyze the air-gap flux voltage and current models' sensitivity to the motor parameters in this paper. A dynamic air-gap current model for EESM based on the equivalent reaction inductance is proposed to solve the parameter dynamic-variant problem caused by the nonlinear magnetic distribution of the EESM. Meanwhile, the comparative analysis of effectiveness caused by linear and nonlinear flux identification errors in the hybrid air-gap flux model of vector control system is carried out. The effectiveness of the nonlinear dynamic model has been verified by simulation and experiment results, which shows its excellent control performance.**

Key words: Nonlinear magnetic field, equivalent reaction inductance, parameter sensitivity, vector control, EESM.

I. INTRODUCTION

With the development of microelectronics technology, power electronics technology, motor technology and control theory, DC motor, double-fed motor, AC asynchronous motor, permanent magnet synchronous motor (PMSM) and electrically excited synchronous motor (EESM) are widely used in high-power applications. Different types of motors have different characteristics as shown in Table I.

TABLE I
COMPARISION OF DIFFERENT TYPES OF HIGH-POWER MOTORS

Type of Motor	Structure	Control	Efficiency	Price
DC motor	Simple	Easy	Low	Cheap
Double-fed motor	Simple	Hard	Medium	Expensive
Asynchronous motor	Medium	Medium	Low	Cheap
PMSM	Simple	Easy	High	Expensive
EESM	Complex	Medium	High	Medium

Among these main types of motor, the EESM discussed in this paper is widely used in mine hoist, transportation, oil rig, steel rolling mill and ship propulsion for its high efficiency and strong overload capability[1-10].

As one typical representative of high-performance control, the air-gap field-oriented vector control solves the problem of decoupling control of EESM theoretically[1,8,14]. The accurate observation of orientation flux is the key to realize decoupling control of magnetic field and torque. The air-gap flux observer can be summarized as the voltage model, which is constructed from the stator voltage and current, and the current model is established by the stator and rotor currents and speed[8]. The model parameters of a traditional air-gap flux observer based on the linear magnetic circuit are constant. However, the stator current of motor will increase gradually with the increase of load, and the air-gap magnetic field presents nonlinear characteristics, which result in dynamic-variant parameters of motor. The flux observation based on the linear magnetic circuit cannot obtain the accurate vector information of the orientation of flux, which affects the control accuracy of a high-performance drive system, and it even leads to system instability and collapse when it is serious.

Aiming at the nonlinear problems of the magnetic field of EESM, a series of analysis has been done by many researchers[10-14,20]. Reference [10] presents that there is d, q axis saturation and alternating magnetic saturation phenomena in a salient pole synchronous motor, and the solutions to the problem of q axis saturation that is difficult to measure are proposed. Meanwhile, the saturation characteristics of q-axis are measured by experiments to verify the existence of q-axis saturation. In reference [11], a triangular mathematical model of EESM based on flux correction method considering the effect of magnetic field nonlinearity is proposed. To reduce the complexity of implicit equations, the i_z model is employed. But the offline calculation for the saturation characteristic and the lookup table must proceed firstly without considering the motor parameter changes. In reference [12], the inductance maps are fitted by polynomials of current variables. They are derived from the flux linkage map obtained from Finite Element Analysis (FEA). It can achieve a good nonlinear prediction of inductances, but the changes of other motor parameters that can influence the system are not discussed. In reference [13], the mathematical model of synchronous motor considering the nonlinear effect of magnetic field is established by using the idea of hidden pole transformation. It is shown that various sets of state variables have a common theoretical background what simplifies the deduction of the saturated model, which is related to the degree of motor saturation, the reference frame system and the state variables. In reference [14], by combining the flux state observer with model reference adaptive system (MRAS), the speed of motor can be identified. The reduced-order observer works as an adjustable model, and the current model flux observation functions as the reference model. But the error of reference model is not considered.

Throughout the existing literature, only the analysis and model construction of the magnetic field nonlinearity of EESM are carried out. However, the influence of magnetic field nonlinearity on vector control and its solution are not studied. Aiming at the dynamic-variant parameters caused by the nonlinear magnetic field distribution of the electrically excited synchronous machine, the corresponding influence on the voltage and current models is analyzed in detail by introducing the error frequency response function

Corresponding Author: Kai Ni

This article has been accepted for publication in a future issue of this journal, but has not been fully edited. Content may change prior to final publication. Citation information: DOI 10.1109/TPEL.2020.2977390, IEEE Transactions on Power Electronics

on the motor parameter related parts of the air-gap flux observers. Moreover, a dynamic air-gap flux model based on equivalent reactive inductance effect for EESM with nonlinear magnetic field is proposed and applied to the vector control system.

The basic structure of this paper is as follows: Firstly, the sensitivity of voltage and current model parameters is analyzed in detail by error frequency response function. Secondly, the dynamic air-gap flux variable parameter model based on equivalent reactive inductance effect is constructed. Then, the simulation and experimental results are analyzed. Finally, the conclusion of this paper is given.

II. SYSTEM OVERVIEW

The researched synchronous motor with damped windings is shown in Fig. 1. The mathematical model of excitation synchronous motor in dq frame system based on double armature reaction theory is shown in Eq. (1)-(6) [1,8].

$$\boldsymbol{u}_{\mathrm{s}} = R_{\mathrm{s}}\boldsymbol{i}_{\mathrm{s}} + \frac{d}{dt}\boldsymbol{\psi}_{\mathrm{s}} + j\omega_{\mathrm{r}}\boldsymbol{\psi}_{\mathrm{s}} \tag{1}$$

$$\boldsymbol{u}_{\mathrm{f}} = R_{\mathrm{f}}\boldsymbol{i}_{\mathrm{f}} + \frac{d}{dt}\boldsymbol{\psi}_{\mathrm{f}} \tag{2}$$

$$\boldsymbol{u}_{\mathrm{D}} = R_{\mathrm{D}}\boldsymbol{i}_{\mathrm{D}} + \frac{d}{dt}\boldsymbol{\psi}_{\mathrm{D}} \tag{3}$$

$$\boldsymbol{\psi}_{\mathrm{s}} = L_{\mathrm{s}\sigma}\boldsymbol{i}_{\mathrm{s}} + \boldsymbol{\psi}_{\mathrm{m}} \tag{4}$$

$$\boldsymbol{\psi}_{\mathrm{f}} = L_{\mathrm{f}\sigma}\boldsymbol{i}_{\mathrm{f}} + \boldsymbol{\psi}_{\mathrm{m}} \tag{5}$$

$$\boldsymbol{\psi}_{\mathrm{D}} = L_{\mathrm{D}\sigma}\boldsymbol{i}_{\mathrm{D}} + \boldsymbol{\psi}_{\mathrm{m}} \tag{6}$$

And $\boldsymbol{\psi}_{\mathrm{m}} = L_{\mathrm{m}}\boldsymbol{i}_{\mathrm{m}}$, $\boldsymbol{i}_{\mathrm{m}} = \boldsymbol{i}_{\mathrm{s}} + \boldsymbol{i}_{\mathrm{f}} + \boldsymbol{i}_{\mathrm{D}}$。

where u, i, ψ, R, and L represent voltage, current, flux, resistance and inductance respectively. σ represents the flux leakage. Subscripts s, m, f, D represent stator, air-gap , excitation and damper windings respectively. d and q represent the components in the dq frame. ω_{r} is the electrical angular velocity of the rotor. θ_{r} is the electrical angular of the rotor. Superscript ^ represents the observed value.

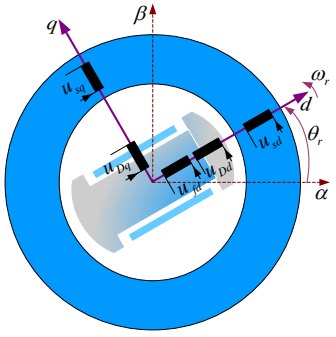

Fig. 1 Model schemes of the electrically excited salient pole synchronous motor

III. SENSITIVITY ANALYSIS OF MOTOR MODEL PARAMETERS

The vector control system diagram of three-level EESM based on air-gap flux orientated is shown in Fig. 2. As the key variable of vector control of EESM, accurate air-gap flux vector information is the basis for high performance control of the system. The parameter sensitivity of voltage and current models is analyzed by introducing the error frequency response function.

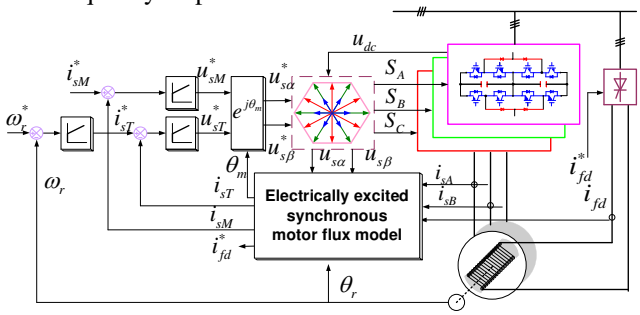

Fig. 2 Vector control system of three-level electrically excited salient pole synchronous motor

A. Sensitivity Analysis of Voltage Model Parameters

The rotor synchronous rotating frame reference system dq is used in Eq.(1)-Eq.(6) while the stator stationary frame reference system αβ is used in Eq.(7) because of its simplicity for applying the air-gap magnetic field voltage model. In the αβ reference system, the air-gap flux voltage model can be obtained from stator resistor and voltage[1],[4],[15], as shown in the follows:

$$\boldsymbol{\psi}_{\mathrm{m}}^{\mathrm{u}} = \frac{1}{p}(\boldsymbol{u}_{\mathrm{s}} - R_{\mathrm{s}}\boldsymbol{i}_{\mathrm{s}}) - L_{\mathrm{s}\sigma}\boldsymbol{i}_{\mathrm{s}} \tag{7}$$

where p=d/dt, is the differential operator, superscript u represents the voltage model, and subscript m represents the air-gap flux.

Eq. (7) shows that the flux identification method based on voltage model is mainly obtained by the induced potential. In the process of observation, the errors of stator resistance and leakage inductance will affect the accuracy of flux observation.

Frequency response function (FRF)[15] is introduced to analyze the effect of parameter estimation on the air-gap flux model, which is derived from the actual value of flux observation accuracy.

By reorganizing Eq.(7), and replacing the real parameters with the estimated ones, the estimated parameter air-gap flux voltage model shown in Eq.(8) can be obtained.

$$\hat{\boldsymbol{\psi}}_{\mathrm{m}}^{\mathrm{u}} = \frac{1}{p}(\boldsymbol{u}_{\mathrm{s}} - \hat{R}_{\mathrm{s}}\boldsymbol{i}_{\mathrm{s}}) - \hat{L}_{\mathrm{s}\sigma}\boldsymbol{i}_{\mathrm{s}} \tag{8}$$

In practice, when the system reaches an equilibrium state, the d-q axes output voltages will level off with small variations. By using a phase voltage reconstruction algorithm[9] and for the sake of simplicity, the impacts of the voltage on the air-gap flux can be ignored when assessing the flux sensitivity to the parameter variations. The other two parts of the air-gap flux observer are sensitive to the motor parameters. The actual value $\Delta\boldsymbol{\psi}_{\mathrm{m}}^{\mathrm{u}}$ and observed value $\Delta\hat{\boldsymbol{\psi}}_{\mathrm{m}}^{\mathrm{u}}$ are expressed as follows, respectively:

$$\Delta\boldsymbol{\psi}_{\mathrm{m}}^{\mathrm{u}} = -(\frac{1}{p}R_{\mathrm{s}} + L_{\mathrm{s}\sigma})\boldsymbol{i}_{\mathrm{s}} \tag{9}$$

$$\Delta\hat{\boldsymbol{\psi}}_{\mathrm{m}}^{\mathrm{u}} = -(\frac{1}{p}\hat{R}_{\mathrm{s}} + \hat{L}_{\mathrm{s}\sigma})\boldsymbol{i}_{\mathrm{s}} \tag{10}$$

From the Eq.(9) and (10), the error frequency response function of the voltage model can be obtained as:

This article has been accepted for publication in a future issue of this journal, but has not been fully edited. Content may change prior to final publication. Citation information: DOI 10.1109/TPEL.2020.2977390, IEEE Transactions on Power Electronics

$$FRF^{u}(p)=\frac{\Delta\hat{\psi}_{m}^{u}}{\Delta\psi_{m}^{u}}=\frac{p\hat{L}_{s\sigma}+\hat{R}_{s}}{pL_{s\sigma}+R_{s}} \tag{11}$$

When a steady unit excitation signal is used for the analysis of the frequency response function, p can be substituted by $j\omega$. Substituting $p=j\omega$, Eq. (12) can be obtained:

$$FRF^{u}(j\omega)=\frac{j\omega\hat{L}_{s\sigma}+\hat{R}_{s}}{j\omega L_{s\sigma}+R_{s}} \tag{12}$$

The amplitude and phase diagrams are shown in Fig. 3, which reflect the influence of stator resistance errors in the voltage model on the observed values of air-gap flux. It can be seen from Fig. 3 that the stator resistance error has some influence on the flux observation accuracy at low speed. With the increase of motor speed, the stator resistor error influence on the flux observation is weakened.

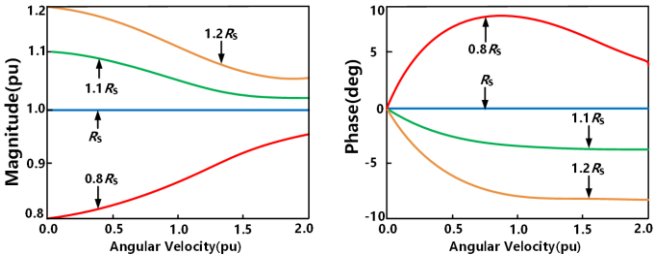

Fig. 3 Voltage model sensitivity analysis on the stator resistance

Fig. 4 is the FRF^{u} response diagram of the effect of stator leakage inductance error on the observed value of air-gap flux. It can be seen from Fig. 4 that with the increase of motor speed, the influence of stator leakage inductance error on the accuracy of air-gap flux observation is gradually enhanced. Compared with the stator resistance error, the stator leakage inductance error has less influence on the voltage model magnitude at lower speed.

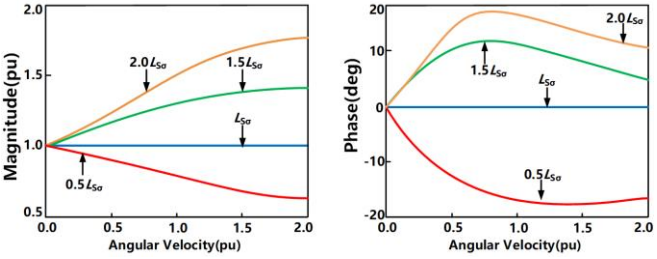

Fig. 4 Voltage model sensitivity analysis on the leakage inductance of the stator

B. Sensitivity Analysis of Current Model Parameters

The expression of air-gap flux current model in the dq frame system can be obtained by Eq. (4), (5), (6).

$$\begin{cases}\psi_{md}^{i}=L_{md}i_{md}=L_{md}(i_{fd}+i_{sd}+i_{Dd})\\ \psi_{mq}^{i}=L_{mq}i_{mq}=L_{mq}(i_{sq}+i_{Dq})\end{cases} \tag{13}$$

where superscript i represents the current model, d and q represent the d and q axis respectively.

Because the currents i_{Dd} and i_{Dq} of the damped winding cannot be obtained directly by measurement[11], considering the short circuits at both ends of the damped winding, the currents $\hat{i}_{Dd}$ and $\hat{i}_{Dq}$ on the d and q axes of the damped winding can be reconstructed by Eq. (3) and (6).

$$\begin{cases}\hat{i}_{Dd}=-\dfrac{L_{md}}{L_{md}+L_{D\sigma d}}\cdot\dfrac{p\tau_{Dd}}{1+p\tau_{Dd}}(i_{sd}+i_{fd})\\ \hat{i}_{Dq}=-(\dfrac{L_{mq}}{L_{mq}+L_{D\sigma q}}\cdot\dfrac{p\tau_{Dq}}{1+p\tau_{Dq}})i_{sq}\end{cases} \tag{14}$$

where $\tau_{Dd}=\dfrac{L_{md}+L_{D\sigma d}}{R_{Dd}}$, and $\tau_{Dq}=\dfrac{L_{mq}+L_{D\sigma q}}{R_{Dq}}$. Eq. (14) is substituted into Eq. (13) to get the following equation:

$$\begin{cases}\psi_{md}^{i}=\dfrac{p\tau_{Dd}L_{md}L_{D\sigma d}+L_{md}(L_{md}+L_{D\sigma d})}{p\tau_{Dd}(L_{md}+L_{D\sigma d})+(L_{md}+L_{D\sigma d})}\cdot(i_{fd}+i_{sd})\\ \psi_{mq}^{i}=\dfrac{p\tau_{Dq}L_{mq}L_{D\sigma q}+L_{mq}(L_{mq}+L_{D\sigma q})}{p\tau_{Dq}(L_{mq}+L_{D\sigma q})+(L_{mq}+L_{D\sigma q})}\cdot i_{sq}\end{cases} \tag{15}$$

The actual and observed values of the air-gap flux, as shown in Eq. (15), are expressed in the vector form, as shown in Eq. (16) and (17) respectively. The block diagram of the air-gap flux current model is shown in Fig. 5.

$$\boldsymbol{\psi}_{m}^{i}=\frac{p\tau_{Ddq}L_{mdq}L_{D\sigma dq}+L_{mdq}(L_{mdq}+L_{D\sigma dq})}{p\tau_{Ddq}(L_{mdq}+L_{D\sigma dq})+(L_{mdq}+L_{D\sigma dq})}\boldsymbol{i}_{m} \tag{16}$$

$$\hat{\boldsymbol{\psi}}_{m}^{i}=\frac{p\hat{\tau}_{Ddq}\hat{L}_{mdq}\hat{L}_{D\sigma dq}+\hat{L}_{mdq}(\hat{L}_{mdq}+\hat{L}_{D\sigma dq})}{p\hat{\tau}_{Ddq}(\hat{L}_{mdq}+\hat{L}_{D\sigma dq})+(\hat{L}_{mdq}+\hat{L}_{D\sigma dq})}\boldsymbol{i}_{m} \tag{17}$$

where, $\boldsymbol{i}_{m}=(i_{fd}+i_{sd})+ji_{sq}$.

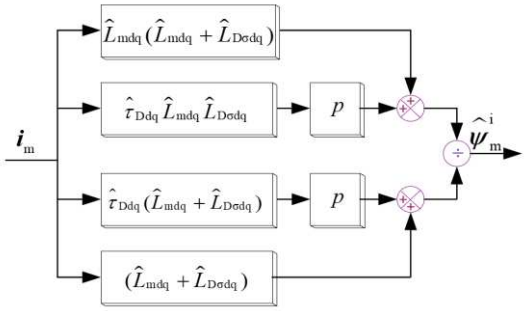

Fig. 5 Air-gap flux based on the current model

The current model error frequency response function FRF^{i} can be obtained from Eq. (16) and (17).

$$FRF^{i}(p)=\frac{\hat{\boldsymbol{\psi}}_{m}^{i}}{\boldsymbol{\psi}_{m}^{i}}=\frac{p^{2}\hat{L}_{3}L_{4}+p(\hat{L}_{2}L_{4}+\hat{L}_{3}L_{1})+\hat{L}_{2}L_{1}}{p^{2}L_{3}\hat{L}_{4}+p(L_{2}\hat{L}_{4}+L_{3}\hat{L}_{1})+L_{2}\hat{L}_{1}} \tag{18}$$

where, $L_{1}=L_{mdq}+L_{D\sigma dq}$, $L_{2}=L_{mdq}(L_{mdq}+L_{D\sigma dq})$

$L_{3}=\tau_{Ddq}L_{mdq}L_{D\sigma dq}$, $L_{4}=\tau_{Ddq}(L_{mdq}+L_{D\sigma dq})$,

$\hat{L}_{1}=\hat{L}_{mdq}+\hat{L}_{D\sigma dq}$, $\hat{L}_{2}=\hat{L}_{mdq}(\hat{L}_{mdq}+\hat{L}_{D\sigma dq})$,

$\hat{L}_{3}=\hat{\tau}_{D\sigma dq}\hat{L}_{mdq}\hat{L}_{D\sigma dq}$, $\hat{L}_{4}=\hat{\tau}_{Ddq}(\hat{L}_{mdq}+\hat{L}_{D\sigma dq})$。

Substituting $p=j\omega$ into Eq. (18), Eq. (19) can be obtained:

$$FRF^{i}(j\omega)=\frac{-\omega^{2}\hat{L}_{3}L_{4}+(j\omega)(\hat{L}_{2}L_{4}+\hat{L}_{3}L_{1})+\hat{L}_{2}L_{1}}{-\omega^{2}L_{3}\hat{L}_{4}+(j\omega)(L_{2}\hat{L}_{4}+L_{3}\hat{L}_{1})+L_{2}\hat{L}_{1}} \tag{19}$$

This article has been accepted for publication in a future issue of this journal, but has not been fully edited. Content may change prior to final publication. Citation information: DOI 10.1109/TPEL.2020.2977390, IEEE Transactions on Power Electronics

The curves of the current model error frequency response function in Fig. 6-8 represent the relative amplitude error and relative phase error of the flux observation caused by the change of the motor parameters clearly. It can be seen from Fig. 6 that the current model is sensitive to the motor mutual inductance parameters L_{md} and L_{mq}, and the amplitude and phase errors are large under low speed conditions. It can be seen from Fig. 7 that the leakage inductances of the damper winding $L_{D\sigma d}$ and $L_{D\sigma q}$ have little influence on the accuracy of the current model observation. It can be seen from Fig. 8 that the time constant of the damper winding has great influence on the accuracy of flux observation at medium speed. Since the damper winding will generate damping current to hinder the flux change during the dynamic process[15], the current model is more sensitive to the error of the motor parameters in the low speed dynamic process.

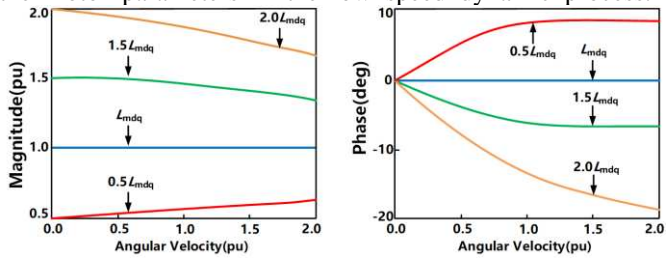

Fig. 6 Current model sensitivity analysis on the mutual inductance

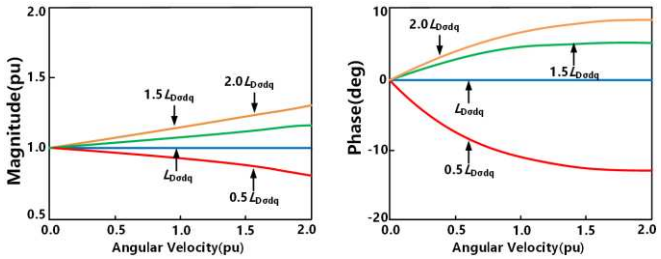

Fig. 7 Current model sensitivity analysis on the leakage inductance of the damper winding

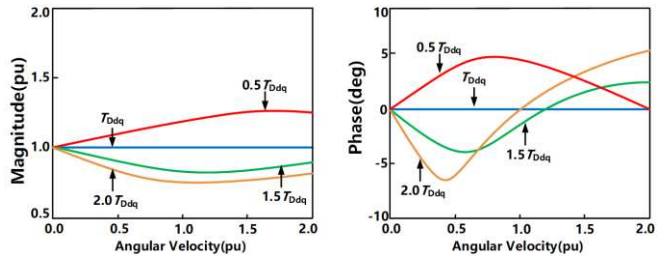

Fig. 8 Current model sensitivity analysis on the time constant of the damper winding

IV.DYNAMIC VARIABLE PARAMETER MAGNETIC FIELD MODEL

It can be seen from the above analysis that the observation accuracy of the voltage and current flux models depends on the accuracy of motor parameters[16-18]. In reference [16], a hybrid air-gap flux model with voltage and current models is used to correct the voltage model by the deviation values of them and overcome the magnetic flux trajectory deviation caused by the stator resistance, leakage inductance error and integral initial value. This algorithm can improve the parameter robustness of the model. However, the observer uses the current model as the implicit expected value and is not included in the forward channel of the feedback loop, so the observation bias of the current model will affect the stability of the entire model. For the high-performance EESM vector control system, the d and q axis magnetic fields can vary in a wide range to satisfy the requirements of the controller[20], and the nonlinearity of the magnetic field is very serious, which is directly reflected in the inductance of the motor model. (The dynamic-variant parameters are usually considered to be less affected by the leakage of the nonlinear magnetic field.) It is necessary to construct a dynamic air-gap flux variable parameter model under nonlinear magnetic field conditions to update the motor parameters in real time and adapt to the magnetic field changes.

In the case of salient-pole motors, due to the geometry of the rotor, one saturation characteristics curve cannot be applied to both d and q axes at the same time[6]. Usually the d-axis saturation characteristics of salient-pole synchronous machines can be determined easily by the conventional open-circuit test with the machines excited from their field windings. On the other hand, the q-axis saturation characteristics of salient-pole synchronous machines cannot be measured by applying a no-load test [21].

According reference [13], ψ_{mq} in Eq.13 may also write

$$\psi_{mq} = L_{md}\frac{L_{mq}}{L_{md}}i_{mq} = L_{md}i'_{mq} \tag{20}$$

where $i'_{mq} = \frac{L_{mq}}{L_{md}}i_{mq}$, since it is assumed the same saturation degree for both d and q axes [22], by defining the salient pole index ξ for EESM, we have

$$\xi^2 = L_{mq0} / L_{md0} = L_{mq} / L_{md} \tag{21}$$

where, L_{md0}, L_{mq0}, L_{md}, L_{mq} are the unsaturation and saturation mutual inductance of d, q axis, respectively.

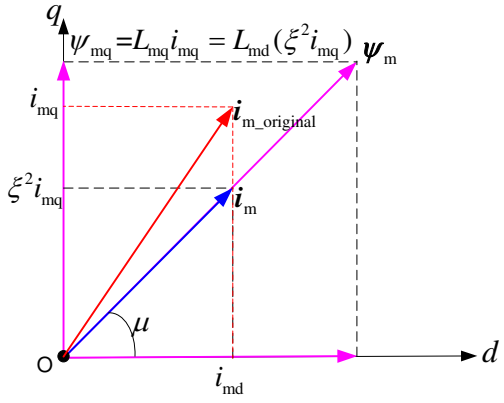

Fig. 9 Current and flux for q axis equivalent

Using the q axis equivalent ideas, the air-gap current and air-gap flux have the same direction, and we denote L_{md}=L_m, the unique steady state equivalent mutual inductance, which varies with the air-gap current i_m, as shown:

This article has been accepted for publication in a future issue of this journal, but has not been fully edited. Content may change prior to final publication. Citation information: DOI 10.1109/TPEL.2020.2977390, IEEE Transactions on Power Electronics

$$\begin{cases} L_{md} = L_m(i_m) \\ L_{mq} = \xi^2 L_m(i_m) \\ L_m = \psi_m / i_m \end{cases} \tag{22}$$

$$\begin{cases} \psi_m = \sqrt{\psi_{md}^2 + \psi_{mq}^2 / \xi^2} \\ i_m = \sqrt{i_{md}^2 + \xi^2 i_{mq}^2} \end{cases} \tag{23}$$

The relationship between ψ_m and air-gap current i_m is shown in the following equation:

$$\begin{cases} \psi_m = L_{md0} i_m & i_m < i_{m\_sat} \\ \psi_m = \dfrac{L_{md0} i_m}{1 + \chi(i_m - i_{m\_sat})} & i_m \geq i_{m\_sat} \end{cases} \tag{24}$$

where, i_{m_sat} is the critical air-gap current value. It is a critical value for the linear magnetic field zone and nonlinera magnetic field zone. And χ is the nonlinear magnetic field curve fitting coefficient. According to the no-load test result for the experiment motor shown in Fig. 10. and the fit curve derived from Eq.(24) $\chi = 0.98$ and $i_{m\_sat} = 0.577$ pu, the measured and fitted saturation characteristic curves can be obtained as shown in Fig. 10.

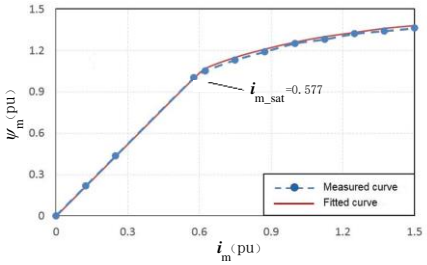

Fig. 10 Measured and fitted saturation characteristics curve of d axis

From Eq.(21) and Eq.(24), the relation between equivalent mutual inductance L_m and air-gap current i_m can be shown as follows:

$$\begin{cases} L_m = L_{md0} & i_m < i_{m\_sat} \\ L_m = \dfrac{L_{md0}}{1 + \chi(i_m - i_{m\_sat})} & i_m \geq i_{m\_sat} \end{cases} \tag{25}$$

Applying the q axis conversion, and according to Eq.(21) and Eq.(22), L_{md}, L_{mq} can be expressed with equivalent mutual inductance L_m, $L_{md} = L_m$, $L_{mq} = \xi^2 L_m$。

From Eq. (13) and (22), the air-gap flux d and q axis components ψ_{md} and ψ_{mq} can be obtained and differentiated，

$$\begin{cases} \dfrac{d\psi_{md}}{dt} = \dfrac{d[L_m(i_m) i_{md}]}{dt} = L_m \dfrac{di_{md}}{dt} + i_{md} \dfrac{dL_m}{dt} \\ \dfrac{d\psi_{mq}}{dt} = \dfrac{d[\xi^2 L_m(i_m) i_{mq}]}{dt} = \xi^2 L_m \dfrac{di_{mq}}{dt} + \xi^2 i_{mq} \dfrac{dL_m}{dt} \end{cases} \tag{26}$$

By differentiating the equivalent mutual inductance L_m in (22):

$$\frac{dL_m}{dt} = \frac{d}{dt}\left(\frac{\psi_m}{i_m}\right) = \frac{\dfrac{d\psi_m}{dt} i_m - \psi_m \dfrac{di_m}{dt}}{i_m^2} = \frac{L_{m\_dyn} \dfrac{di_m}{dt} - L_m \dfrac{di_m}{dt}}{i_m} \tag{27}$$

where, $L_{m\_dyn} = d\psi_m / di_m$ is the dynamic tangent inductance as shown in Eq. (25).

The differential value of the air-gap current i_m is expressed as:

$$\frac{di_m}{dt} = \frac{d}{dt}\left(\sqrt{i_{md}^2 + \xi^2 i_{mq}^2}\right) = \frac{1}{|\boldsymbol{i}_m|}\left(i_{md} \frac{di_{md}}{dt} + \xi^2 i_{mq} \frac{di_{mq}}{dt}\right) \tag{28}$$

The derivative of equivalent mutual inductance to time can be obtained by combining Eq. (27) and (28), which is shown as:

$$\frac{dL_m}{dt} = (L_{m\_dyn} - L_m) \frac{1}{|\boldsymbol{i}_m|^2}\left(i_{md} \frac{di_{md}}{dt} + \xi^2 i_{mq} \frac{di_{mq}}{dt}\right) \tag{29}$$

By substituting Eq. (28) and (29) into Eq. (26), the integrals on both sides of Eq. (26) are shown as:

$$\begin{cases} \psi_{md} = L_{dd} i_{md} + L_{dq} i_{mq} \\ \psi_{mq} = L_{qq} i_{mq} + \xi^2 L_{qd} i_{md} \end{cases} \tag{30}$$

$$\begin{cases} L_{dd} = L_{m\_dyn} \cos^2 \mu + L_m \sin^2 \mu \\ L_{qq} = \xi^2 (L_{m\_dyn} \cos^2 \mu + L_m \sin^2 \mu) \\ L_{dq} = L_{qd} = \xi^2 (L_{m\_dyn} - L_m) \sin \mu \cos \mu \end{cases} \tag{31}$$

$$\begin{cases} \sin \mu = \xi^2 i_{mq} / |\boldsymbol{i}_m| \\ \cos \mu = i_{md} / |\boldsymbol{i}_m| \end{cases} \tag{32}$$

where, L_{dd}, L_{qq}, L_{dq}, L_{qd}, μ are the d, q axis dynamic inductance, dynamic cross-inductance and flux angle.

It can be seen from the Eq. (30), (31) and (32) that the changes in the air-gap currents i_{md} and i_{mq} will cause nonlinear changes in the dynamic inductances L_{dd} and L_{qq} of the d and q axes and the dynamic crossover inductances L_{dq} and L_{qd}.

It can be seen from Fig. 11(a)(b) that as the air-gap current increases, the nonlinearity of the magnetic field increases, and L_{md} and L_{mq} show decreasing trends. The dynamic inductance reflected in Fig. 11(c)(d) also changes as the nonlinearity of the magnetic field changes. It can be seen from Fig. 11(e) that there is a serious nonlinear coupling between the d, q axis inductances in the dynamic process.

Combining Eq. (27), it can be seen that when the amplitude of the air-gap current $\boldsymbol{i}_m$ is smaller than the critical air-gap current value i_{m_sat}, the dynamic tangent inductance $L_{m\_dyn} = L_m$、$L_{dd} = L_{md}$、$L_{qq} = L_{mq}$、$L_{dq} = L_{qd} = 0$，At this moment, the nonlinear magnetic field model returns to the linear magnetic field model, and the proposed nonlinear magnetic field dynamic model is also applicable to linear magnetic field conditions. Further simulation and experiment will proceed to verify the validity of the model.

This article has been accepted for publication in a future issue of this journal, but has not been fully edited. Content may change prior to final publication. Citation information: DOI 10.1109/TPEL.2020.2977390, IEEE Transactions on Power Electronics

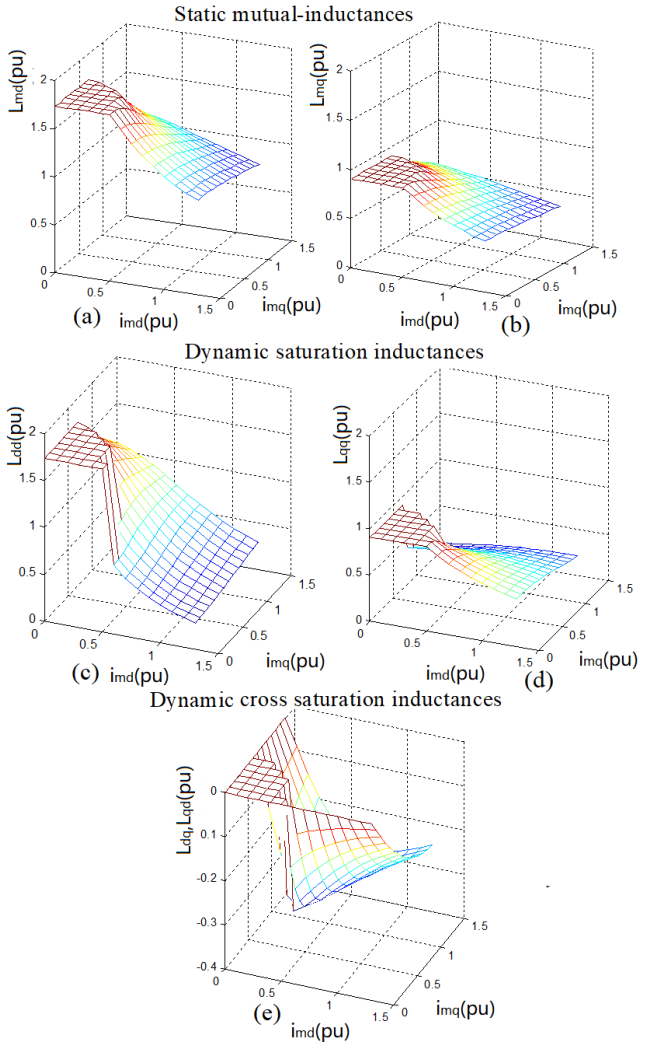

Fig. 11 Key parameters as functions of the air-gap currents in d、q axis

Based on the analysis above, the dq axes currents of the reconstructed damped windings under the nonlinear magnetic field are as follows:

$$\begin{cases} \hat{i}_{\mathrm{Dd}} = -\dfrac{\dfrac{L_{\mathrm{dd}}+L_{\mathrm{D\sigma d}}}{R_{\mathrm{Dd}}}\left[\left(\dfrac{L_{\mathrm{dd}}}{L_{\mathrm{dd}}+L_{\mathrm{D\sigma d}}}\right)p(i_{\mathrm{sd}}+i_{\mathrm{fd}})+\dfrac{L_{\mathrm{dq}}}{L_{\mathrm{dd}}+L_{\mathrm{D\sigma d}}}p(i_{\mathrm{sq}}+\hat{i}_{\mathrm{Dq}})\right]}{\left[1+\dfrac{p(L_{\mathrm{dd}}+L_{\mathrm{D\sigma d}})}{R_{\mathrm{Dd}}}\right]} \\ \hat{i}_{\mathrm{Dq}} = -\dfrac{\dfrac{L_{\mathrm{qq}}+L_{\mathrm{D\sigma q}}}{R_{\mathrm{Dq}}}\left[\left(\dfrac{L_{\mathrm{qq}}}{L_{\mathrm{qq}}+L_{\mathrm{D\sigma q}}}\right)pi_{\mathrm{sq}}+\dfrac{\xi^2 L_{\mathrm{qd}}}{L_{\mathrm{qq}}+L_{\mathrm{D\sigma q}}}p(i_{\mathrm{sd}}+i_{\mathrm{fd}}+\hat{i}_{\mathrm{Dd}})\right]}{\left[1+\dfrac{p(L_{\mathrm{qq}}+L_{\mathrm{D\sigma q}})}{R_{\mathrm{Dq}}}\right]} \end{cases} \tag{33}$$

Fig. 12 is the comparison result of the damper winding currents reconstructed by the linear magnetic field and the nonlinear magnetic field model shown by Eq. (14) and (33) respectively. It can be seen from the figure that the d, q axis damper winding currents reconstructed by the nonlinear magnetic field model $\hat{i}_{\mathrm{Dd\_nonlinear}}$, $\hat{i}_{\mathrm{Dq\_nonlinear}}$ have much higher accuracy than the linear magnetic field model reconstructed currents $\hat{i}_{\mathrm{Dd\_linear}}$, $\hat{i}_{\mathrm{Dq\_linear}}$. Subscripts linear, nonlinear represent linear and nonlinear magnetic field model in Fig. 12 respectively.

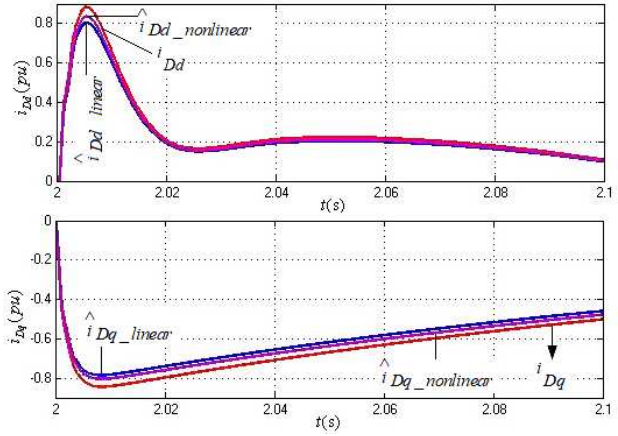

Fig. 12 Comparison of the damper winding currents estimation accuracy

By substituting Eq. (33) into (30), the air-gap flux current model under any magnetic field condition can be obtained as (34) and shown in Fig. 13.

$$\begin{cases} \psi_{\mathrm{md}}^{\mathrm{i}} = L_{\mathrm{dd}}(i_{\mathrm{fd}}+i_{\mathrm{sd}}+\hat{i}_{\mathrm{Dd}})+L_{\mathrm{dq}}(i_{\mathrm{sq}}+\hat{i}_{\mathrm{Dq}}) \\ \psi_{\mathrm{mq}}^{\mathrm{i}} = L_{\mathrm{qq}}(i_{\mathrm{sq}}+\hat{i}_{\mathrm{Dq}})+\xi^2 L_{\mathrm{qd}}(i_{\mathrm{fd}}+i_{\mathrm{sd}}+\hat{i}_{\mathrm{Dd}}) \end{cases} \tag{34}$$

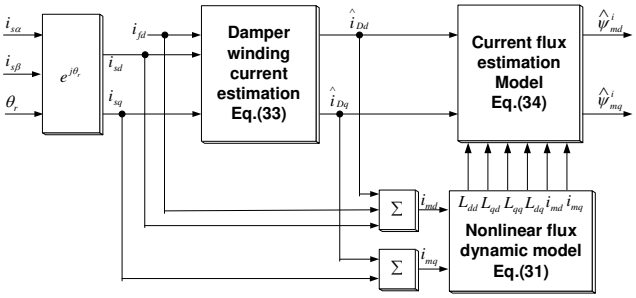

Fig. 13 Dynamic current model of the nonlinear magnetic field

V.SIMULATION AND ANALYSIS OF EXPERIMENT RESULTS

To verify the effectiveness of the nonlinear magnetic field dynamic model of EESM, a simulation model and experimental platform of the vector control system for the EESM with a dual three-level PWM power converter are established. And a Siemens 6RA70-driven DC motor is used as the load of the control system, as shown in Fig. 14. The motor parameters are the same as those used in the simulation, which are listed in Table II.

TABLE II
SALIENT-POLE SYNCHRONOUS MOTOR PARAMETERS

Parameter	Symbols/ Units	Value
Rated power	P_{n}/kW	225
Stator rated voltage	U_{n}/V	380
Stator rated current	I_{n}/A	410
Rotor rated current	I_{fn}/A	334
Motor frequency	f_{n}/Hz	50
pole pairs	p	5
Stator resistance	R_{s}/Ω	0.014181
Stator leakage inductance	$L_{\mathrm{s\sigma}}$/H	0.000218
d axis magnetic field inductance	$L_{\mathrm{md\_line}}$/H	0.002738

q axis magnetic field inductance	L_{mq_line}/H	0.001329
Damping winding d axis resistance	R_D/Ω	0.02164
Damping winding d axis leakage inductance	$L_{Dσ}$/H	0.000327
Damping winding q axis resistance	R_Q/Ω	0.03397
Damping winding q axis leakage inductance	$L_{Qσ}$/H	0.00048
Critical air-gap current	i_{m_sat}/A	285

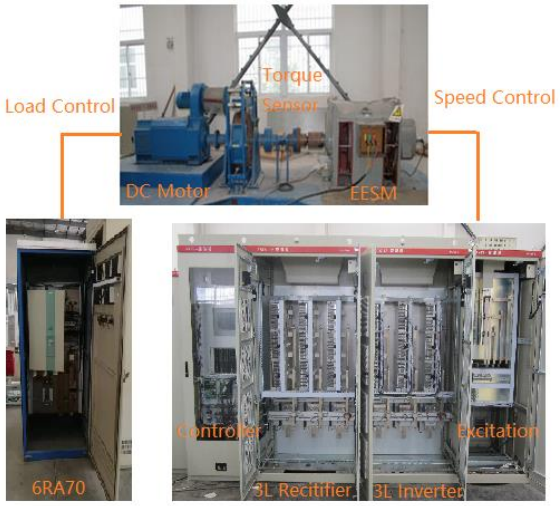

Fig. 14 Photographs of experimental environments

The following simulations and experiments use the voltage model as an air-gap flux trainer when analyzing the nonlinear magnetic field dynamic current model[23]. Considering the stability problem at low speed, the motors are all running at high speed. In the analysis process, the control quantities obtained by the linear and the nonlinear magnetic field current models are indicated by subscripts "linear" and "nonlinear" respectively.

A. Simulation Analysis of Nonlinear Dynamic-Variant Parameter Current Model

A vector control system of a three-level electrically excited salient pole synchronous motor can be established based on Eq.(15) and Eq.(34) as Fig. 2 to verify the accuracy of the linear and nonlinear air-gap flux current model, respectively. The comparison of the accuracy for air-gap flux, rotor excitation current and stator torque current, rotor excitation current and stator d, q axis current, torque and air-gap flux amplitude between the linear magnetic field and that of the nonlinear magnetic field current model have been completed in Matlab/Simulink (R2014a).

The results are shown in Fig. 15. The linear magnetic field current model cannot accurately observe the air-gap flux because the magnetic field enters the nonlinear region, which is equivalent to the dynamic-variant characteristic of the induced inductance in the figure. There is an error between $\hat{\psi}^{i}_{mα\_linear}$, $\hat{\psi}^{i}_{mβ\_linear}$ and the real air-gap fluxes $\psi_{mα}$, $\psi_{mβ}$, The air-gap fluxes $\psi_{mα}$, $\psi_{mβ}$ observed by the nonlinear magnetic field current model have high observation accuracy.

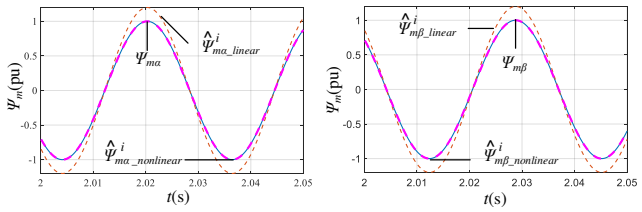

Fig. 15 The observation precision comparison of air-gap flux

The relative error for linear air-gap flux model is shown as following and the maximum error is 25% @ 2.03s as shown，which may lead to system fault.

TABLE III
ERROR OF LINEAR AIR-GAP FLUX MODEL

Time(s)	2.00	2.01	2.02	2.03	2.04	2.05
$\psi_{mα}$ (pu)	-0.73	-0.41	0.98	-0.08	-0.25	0.81
$\hat{\psi}^{i}_{mα\_linear}$ (pu)	-0.86	-0.51	1.18	-0.10	-0.29	0.96
Error (%)	17	24	20	25	16	18
$\psi_{mβ}$(pu)	0.65	-0.81	-0.11	1.01	-0.51	-0.66
$\hat{\psi}^{i}_{mβ\_linear}$ (pu)	0.77	-0.95	-0.13	1.18	-0.60	-0.77
Error (%)	18	17	18	16	17	16

As shown in Fig. 2, the current model in the hybrid air-gap flux model of the EESM vector control system adopts a linear magnetic field current model and a nonlinear magnetic field current model, respectively. And it adopts a flux closed-loop control strategy. The load of motor is increased from zero to the rated value at t=2s. Fig. 16(a) shows the variation of rotor excitation current. It can be seen from the simulation results that the nonlinear magnetic field will cause the inductance parameters of the motor to change. The linear field current model will reduce the rotor excitation current i_{fd} with respect to the nonlinear magnetic field current model from 1.75 pu to 1.52 pu, thus the true air-gap magnetic flux is reduced.

At the same time, to balance the load torque, the stator torque current i_{sT} is increased from 0.92 pu to 1.05 pu with respect to the nonlinear magnetic field current model. Fig. 16(b) shows the process of changing the rotor exciting current i_{fd} and the stator currents i_{sd}, i_{sq} during the sudden load increase. Due to the influence of armature reaction, i_{sd} is reduced, and the air-gap magnetic flux is demagnetized. In order to balance the load torque, the stator torque current i_{sT} increases instantaneously, and i_{sq} increases too. Under the closed-loop control of the flux, i_{fd} is increased to compensate for the demagnetization of i_{sd}. Under the influence of nonlinear magnetic field, if the linear magnetic field current model is used, i_{sq} will increase from 0.89 pu to 0.95 pu with respect to the nonlinear magnetic field current model, and i_{sd} will increase from 0.23 pu to 0.35 pu with respect to the nonlinear magnetic field current model to maintain the torque current unchanged. It can be seen from Fig. 16(c) that when applying the linear magnetic field current model, the air-gap flux exhibits a small amplitude attenuation oscillation, compared with the case of applying the nonlinear magnetic field current model, and the electromag-

This article has been accepted for publication in a future issue of this journal, but has not been fully edited. Content may change prior to final publication. Citation information: DOI 10.1109/TPEL.2020.2977390, IEEE Transactions on Power Electronics

netic torques in the two models are slightly different due to the air-gap flux oscillation.

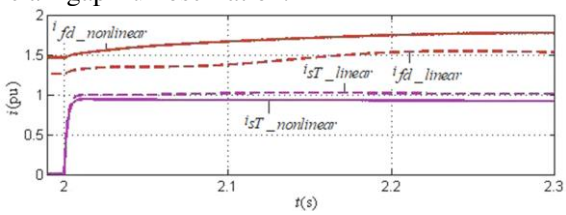

(a) Comparison of rotor excitation current and stator torque current

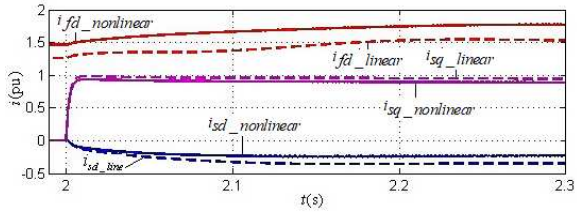

(b) Comparison of rotor excitation current and stator d, q axis current

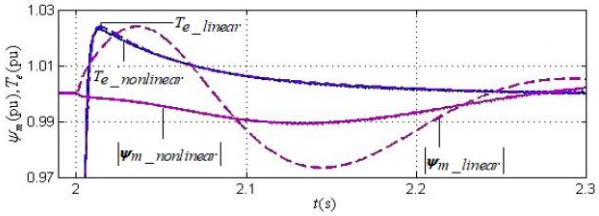

(c) Comparison of torque and air-gap flux amplitude

Fig. 16 Comparing simulation waveforms of the systems' running volume

B. Experiment Analysis of Nonlinear Dynamic-Variant Parameter Model

In the comparison experiment of the two airgap models shown in Fig. 17, the air-gap flux observer uses the MT[23] voltage model, where the DC motor armature current is 100A, and the motor speed under steady state operation is 300 rpm. It can be seen from the figure that there is an error between the observed values of the linear magnetic field current model and the observed values of the MT[23] type voltage model. The nonlinear dynamic model has a good agreement with the observed values of the voltage model. The experiment is consistent with the simulation, and the accuracy of the nonlinear dynamic variable parameter model of the EESM is further verified.

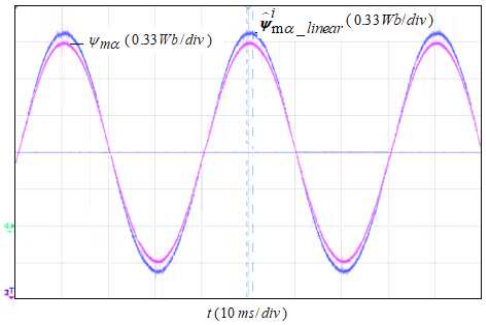

(a) Linear current model

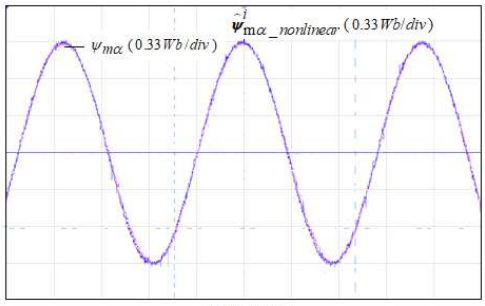

(b) Nonlinear current model

Fig. 17 Experimental waveforms of linear and nonlinear current model

C. Experiment Analysis of Hybrid Air-gap Model With Nonlinear Dynamic-Variant Parameter Current Model

Based on the proposed nonlinear air-gap flux current model considering the influence of saturation effect, a more accurate current flux model can be achieved. Further, it is can be introduced into the hybrid air-gap flux model consisting of the voltage and current models to compensate the voltage model observation error as shown in Fig. 18 [1][9][17]. The current model in the figure is discussed above.

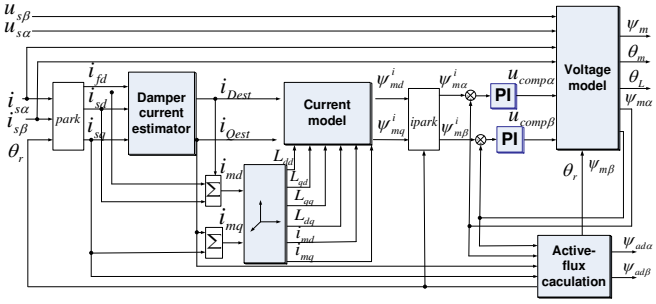

Fig. 18 Hybrid air-gap flux model diagram

Fig. 19 (a) shows the running experimental waveform of the system when the linear current model is used in the hybrid air-gap flux model. It can be seen from Fig. 19(a) that as the load torque increases, the motor torque current increases, and the nonlinear magnetic field effect becomes more serious, causing the motor model parameters to change. The current model constructed according to the linear magnetic circuit cannot correctly identify the value and direction of the flux. When the peak value of stator torque current i_{sT} reaches 150A, the stator current excitation component i_{sM}, the stator current torque component i_{sT} and the flux amplitude $|\hat{\psi}_{m\_linear}|$ all show diverging trends. When i_{sT} reaches 200A, the system is unstable.

Fig. 19 (b) shows the operating waveform of the system when the hybrid air-gap flux model uses a nonlinear dynamic variant parameters current model. It can be seen from the figure that during the load increase process, the rotor current changes in accordance with the motor running law, and the flux amplitude $|\hat{\psi}_{m\_nonlinear}|$ tracks the expected value, and the system runs smoothly, which verifies that the model has good observation accuracy.

This article has been accepted for publication in a future issue of this journal, but has not been fully edited. Content may change prior to final publication. Citation information: DOI 10.1109/TPEL.2020.2977390, IEEE Transactions on Power Electronics

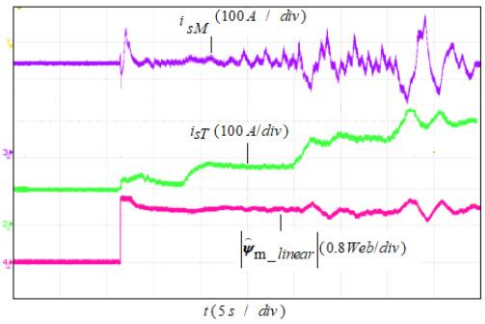

(a) With hybrid air-gap flux model using linear current model

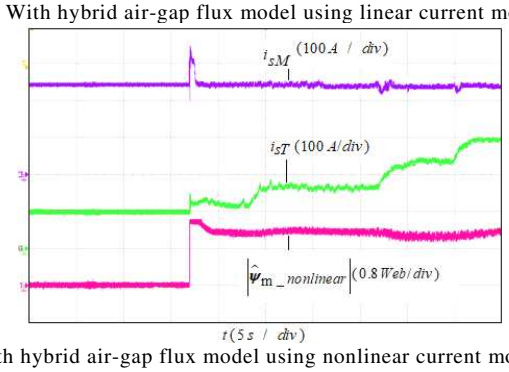

(b) With hybrid air-gap flux model using nonlinear current model

Fig. 19 Comparing experimental waveforms of system stability

Fig. 20 is the comparative waveform of the measured torque response with a torque sensor when the linear and the nonlinear air-gap current flux models are used in the hybrid air-gap flux model respectively. It can be seen from Fig. 19 that in the process of sudden load increase, the parameters of the linear magnetic field current model keep unchanged, resulting in the oscillation of the torque response until the system fault protection is activated. In contrast, the nonlinear magnetic field current model parameters update with the nonlinear magnetic characteristics in real time to adapt to the change of load. And the motor torque can reach the new steady state within 50ms for a 2400 N·m change as shown in Fig. 20.

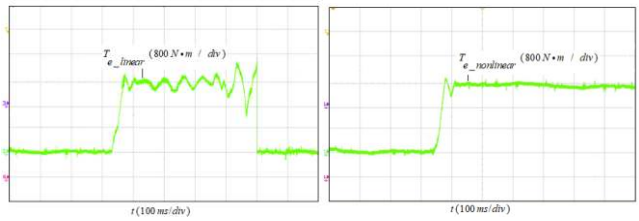

(a) Torque response in linear model (b) Torque response in nonlinear model

Fig. 20 Comparing experimental waveforms of torque response

As can be seen from Fig. 21, $\hat{\psi}_{m\alpha\_nonlinear}$ is the instantaneous value of α axis component flux observed by the hybrid air-gap flux model based on nonlinear air-gap flux current model. In the process of sudden loading, the amplitude of $\hat{\psi}_{m\alpha\_nonlinear}$ and air-gap flux angle are almost unaffected in the dynamic process, the stator torque current i_{sT} from 0A to -250A but the speed n changes only 5 rpm temporally and reach to new steady state within 150ms , which ensures the accuracy of flux orientation. Therefore, the system has excellent control performance.

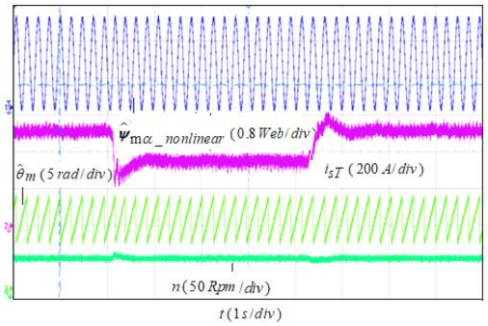

Fig. 21 Experimental waveforms with sudden load during system operation

Fig. 22 shows the waveforms of i_{sA}, i_{sB} and i_{sC} of stator three-phase current in steady-state operation with load. It can be seen from the figure that the current waveforms have a higher sinusoidal degree and lower distortion rate when the hybrid air-gap flux model using the nonlinear current model is employed in the vector control system compared with that of the nonlinear current model.

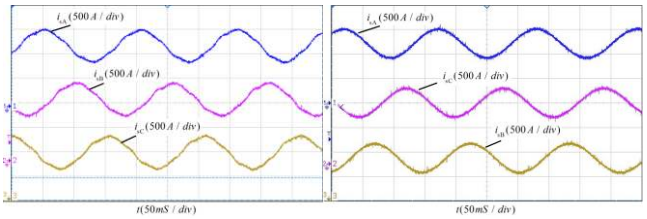

(a)Current waveforms in linear model (b)Current waveforms in nonlinear model

Fig. 22 Experimental waveforms with load during steady-state operation

VI.CONCLUSION

In this paper, the parameter sensitivity of two air-gap flux models in the vector control system of electric excitation synchronous motor is analyzed by introducing the error frequency response function. With the enhancement of the nonlinearity of magnetic field, the dynamic-variant characteristics of inductance parameters are induced. According to the current model constructed by the linear magnetic field, the air-gap flux cannot be accurately observed. To solve this problem, a dynamic-variant parameter model of the nonlinear magnetic field of the EESM is proposed, which can observe the air-gap flux accurately. The results of simulation and experiment are analyzed, and the following conclusions can be drawn:

1. The dynamic-variant parameters caused by the nonlinear magnetic field have little influence on the voltage model. The influence of stator resistance can be compensated by the current model. The current model is sensitive to the parameters.

2. Aiming at the problem that linear magnetic field current model cannot observe the air-gap flux under the condition of nonlinear magnetic field accurately, a dynamic-variable parameter current model of nonlinear magnetic field is proposed, which can accurately observe air-gap flux under the arbitrary magnetic field environment and has good parameter robustness.

3. According to the comparative analysis, the effective implementation of vector control system for EESM is guaranteed based on the hybrid air-gap flux model using dynamic-variant parameter nonlinear air-gap current model proposed in this paper. Besides, it has excellent torque response characteristics.

REFERENCES

[1] C. Li, Adjusting speed of synchronous motor, 2nd ed., Science Press, Beijing, 2006.

[2] T. J. Besselmann, S. Almér and H. J. Ferreau, "Model Predictive Control of Load-Commutated Inverter-Fed Synchronous Machines," in *IEEE Transactions on Power Electronics*, vol. 31, no. 10, pp. 7384-7393, Oct. 2016.

[3] Y. Nie, I. P. Brown and D. C. Ludois, "Deadbeat-Direct Torque and Flux Control for Wound Field Synchronous Machines," in *IEEE Transactions on Industrial Electronics*, vol. 65, no. 3, pp. 2069-2079, March 2018.

[4] Y. Zhou and S. Long, "Sensorless Direct Torque Control for Electrically Excited Synchronous Motor Based on Injecting High-Frequency Ripple Current Into Rotor Winding," in *IEEE Transactions on Energy Conversion*, vol. 30, no. 1, pp. 246-253, March 2015.

[5] Y. Sangsefidi, S. Ziaeinejad and A. Mehrizi-Sani, "Sensorless Speed Control of Synchronous Motors: Analysis and Mitigation of Stator Resistance Error," in *IEEE Transactions on Energy Conversion*, vol. 31, no. 2, pp. 540-548, June 2016.

[6] J. Luukko, M. Niemela and J. Pyrhonen, "Estimation of the flux linkage in a direct-torque-controlled drive," in *IEEE Transactions on Industrial Electronics*, vol. 50, no. 2, pp. 283-287, April 2003.

[7] J. Kou, Q. Gao, K. Xu and D. Xu, "A Sensorless Rotor Position Estimation Method Based on the Field Current Harmonic for an LCI-Fed EESM," in *IEEE Transactions on Industrial Electronics*, vol. 66, no. 4, pp. 2561-2569, April 2019.

[8] G. Tan, X. Wu, H. Li, W. Jing, M. Liu, "Vector Control System of Electrically Excited Synchronous Motor Fed by Back-to-Back Dual Three-Level Converter," in *Transactions of China Electrotechnical Society*, Vol.26, no. 3 2011, 26(3):36-43.

[9] Y. Han, High-power back-to-back three-level converter control system, Beijing University of Aeronautics and Astronautics Press, Beijing, 2017.

[10] N. C. Kar and A. M. El-Serafi, "Measurement of the saturation characteristics in the quadrature axis of synchronous machines," in *IEEE Transactions on Energy Conversion*, vol. 21, no. 3, pp. 690-698, Sept. 2006.

[11] L. Wang, J. Jatskevich, N. Ozog and A. Davoudi, "A Simple Explicit Method of Representing Magnetic Saturation of Salient-Pole Synchronous Machines in Both Rotor Axes Using Matlab-Simulink," *2007 Canadian Conference on Electrical and Computer Engineering*, Vancouver, BC, 2007, pp. 256-259.

[12] I. Jeong, B. Gu, J. Kim, K. Nam and Y. Kim, "Inductance Estimation of Electrically Excited Synchronous Motor via Polynomial Approximations by Least Square Method," in *IEEE Transactions on Industry Applications*, vol. 51, no. 2, pp. 1526-1537, March-April 2015.

[13] A. Campeanu and M. Badica, "A New Approach of Modeling the Saturated Induction and Synchronous Salient Pole Machines," *2006 CES/IEEE 5th International Power Electronics and Motion Control Conference*, Shanghai, 2006, pp. 1-7.

[14] P. Dai, Y. Lv, N. Xu and H. Xie, "Speed sensorless control of electrically excited synchronous motor based on the reduce-order state observer flux observation," *2016 IEEE 11th Conference on Industrial Electronics and Applications (ICIEA)*, Hefei, 2016, pp. 2009-2014.

[15] P. L. Jansen and R. D. Lorenz, "A physically insightful approach to the design and accuracy assessment of flux observers for field oriented induction machine drives," in *IEEE Transactions on Industry Applications*, vol. 30, no. 1, pp. 101-110, Jan.-Feb. 1994.

[16] J. A. Antonino-Daviu, M. Riera-Guasp, J. Pons-Llinares, J. Roger-Folch, R. B. Pérez and C. Charlton-Pérez, "Toward Condition Monitoring of Damper Windings in Synchronous Motors via EMD Analysis," in IEEE Transactions on Energy Conversion, vol. 27, no. 2, pp. 432-439, June 2012.

[17] X. Wu, G. Tan, J. Song, H. Li. "Electrically excited synchronous motor vector control based on hybrid air-gap flux estimator," in *Electric Machines and Control*, Vol. 14, no. 3, pp. 62-67, Mar. 2010.

[18] G. Andreescu, C. I. Pitic, F. Blaabjerg and I. Boldea, "Combined Flux Observer With Signal Injection Enhancement for Wide Speed Range Sensorless Direct Torque Control of IPMSM Drives," in *IEEE Transactions on Energy Conversion*, vol. 23, no. 2, pp. 393-402, June 2008.

[19] Jun Hu and Bin Wu, "New integration algorithms for estimating motor flux over a wide speed range," in *IEEE Transactions on Power Electronics*, vol. 13, no. 5, pp. 969-977, Sept. 1998.

[20] Y. He, J. Liu, "Study on Cross Saturation Main Maghetic Circuit Based on Synchronous Generator Model," Journal of Changsha University of Electric Power (Natural Science), vol.21, no.3, pp. 6-11, Aug. 2006.

[21] I. Iglesias, L. Garcia-Tabares and J. Tamarit, "A d-q model for the self-commutated synchronous machine considering the effects of magnetic saturation," in *IEEE Transactions on Energy Conversion*, vol. 7, no. 4, pp. 768-776, Dec. 1992.

[22] A. M. El-Serafi and N. C. Kar, "Methods for determining the q-axis saturation characteristics of salient-pole synchronous machines from the measured d-axis characteristics," in *IEEE Transactions on Energy Conversion*, vol. 18, no. 1, pp. 80-86, March 2003.

[23] X. Ma, X. Wei, "Voltage Model of Digital Vector Control and Direct Torque Control Systems," in *Transactions of China Electrotechnical Society*, Vol.19, no. 3, pp. 65-69, Mar. 2004.

Yaofei Han (S'07-M'17) was born in Henan, China. He received the M.S. in 2005 and his Ph.D. in 2010, in power electronics and drives from China University of Mining and Technology respectively. He had been an associate professor at Henan University of Urban Construction since 2012, served in this capacity from 2010 to 2019. He was with the School of Electrical and Computer Engineering, Virginia Polytechnic Institute and State University (VT), as a visiting scholar from 2017 to 2019. Currently, he is a faculty member of Shanghai Jiao Tong University. His research interests include multi-level power converter for power conversion and motor control, high-efficiency converter for renewable power conversion system.

Xuanqin Wu was born in Fujian, China. He received the Ph.D. in 2011, in power electronics and power drives from China University of Mining and Technology. In 2011, he joined China University of Mining as a teacher. In 2015, he then joined the Shenzhen INVT Electric Co., Ltd as the Power Electronics Scientist, where he is the chief manager of Future Research Department. His research interests include multi-level power converter for power conversion and motor control, grid connected inverters.

Guofeng He (M'14) received the B.S. degree in mechanical and electronic engineering from Luoyang Institute of Technology, Luoyang, China in 1996 and M.S. degree in electrical engineering from Shandong University, Shandong China, in 2004. He received Ph.D. from the Department of Electrical Engineering, Zhejiang University, Hangzhou, China, in 2014. He is currently a Faculty Member of Henan University of Urban Construction. His research interests include digital control of parallel UPS system, motor control and grid inverter.

Yihua Hu (M'13-SM'15) received the B.S. degree in electrical engineering in 2003, and the Ph.D. degree in power electronics and drives in 2011, both at China University of Mining and Technology. Between 2011 and 2013, he was with the College of Electrical Engineering, Zhejiang University as a Postdoctoral Fellow. Between 2013 and 2015, he worked as a Research Associate at the power electronics and motor drive group, the University of Strathclyde. Between 2016 and 2019, he was a Lecturer at the Department of Electrical Engineering and Electronics, University of Liverpool (UoL). Currently, he is a Reader at Electronics Engineering Department at The University of York (UoY). His research interests include renewable generation, power electronics converters & control, electric vehicle, more electric ship/aircraft, smart energy system and non-destructive test technology. He is the associate editor of IEEE Transactions on Industrial Electronics, IET Renewable Power Generation, IET Intelligent Transport Systems and Power Electronics and Drives.

This article has been accepted for publication in a future issue of this journal, but has not been fully edited. Content may change prior to final publication. Citation information: DOI 10.1109/TPEL.2020.2977390, IEEE Transactions on Power Electronics

Kai Ni (S'17-M'20) was born in Jiangsu, China. He received the B.Eng. (Hons) degree and Ph.D. degree in Electrical Engineering from the University of Liverpool, Liverpool, UK, in 2016 and 2019, respectively. He joined the School of Electrical and Electronic Engineering at Huazhong University of Science and Technology from Dec. 2019 as a postdoctoral researcher. His research interests include modelling, control and stability analysis of doubly-fed induction machines, power electronic converters, and shipboard power systems.